Proceedings of the 21st ICSMGE, Vienna, Austria, 14 – 19 June 2026. Pistrol, Adam & Schweiger (eds.)
Published by: ÖGG, Austrian Society for Geomechanics, Salzburg, Austria, ISBN 978-3-9503898-4-5
https://doi.org/10.53243/ICSMGE2026-150

Modelling the installation and operational load response of drag embedment anchors in clay in a geotechnical centrifuge

Duy Anh Dao, Jürgen Grabe
Institute of Geotechnical Engineering and Construction Management, TU Hamburg, Germany, duy.anh.dao@tuhh.de

Anderson Peccin da Silva, Dirk A. de Lange, Suzanne J.M. van Eekelen
Deltares, Netherlands

ABSTRACT: This research investigates the offshore soil-structure interaction of drag embedment anchors (DEAs) for floating offshore wind turbines. Centrifuge tests were conducted with a scale of 1:100 to simulate the trajectory of DEAs and to determine the anchor forces under installation, storm-induced, and pull-out loads. Stainless steel anchor models were 3D-printed with fluke-shank angles of 45 °. The test program involved four tests on two soil samples prepared with kaolin clay. Each sample had specified load displacement sequences covering installation (embedding the anchor by pulling the mooring line), storm scenarios (applying sinusoidal loading), and pull-out, to assess the anchor behaviour under different sequences of loading magnitudes. Post-testing procedures included dissecting soil samples and conducting high-resolution 3D scans, providing visualisations of the anchor's trajectory in clay. These scans, supplemented by CloudCompare analysis, allowed for drag depth assessments. The purpose of the study was to obtain physical data to refine numerical DEA predictive models. The results suggest that the studied sequence variation of load magnitudes minimally affected anchor kinematics. Furthermore, it was shown that for approximating the anchor force, the drag distance is negligible, enabling the estimation of the anchor force primarily from the penetration depth, based on a logarithmic fit for the specific anchor.

KEYWORDS: drag embedment anchor (DEA), floating offshore wind turbines, centrifuge modelling, clay

1 INTRODUCTION

The stability of floating offshore structures depends on the performance of station-keeping systems, such as drag embedment anchors (DEAs). Growing deployment of floating facilities will increase requirements for anchor number and efficiency (Cerfontaine et al., 2023; Gourvenec, 2024). Effective DEA design, however, requires an understanding of anchor-seabed interaction under realistic loading histories. Most published work emphasises anchor-chain integrity, whereas the soil-anchor mechanisms that control system safety remain less explored (Hong et al., 2023).

The present study provides centrifuge data linking DEA kinematics during embedment to subsequent load-displacement response under operational loading and pull-out. The experiments support the validation of numerical models developed for DEA behaviour, extending preliminary models reported by Dao et al (2022a, 2022b, 2023) Dao and Dicke (2023) and Dao and Grabe (2024).

Centrifuge investigations of DEA behaviour in clay remain limited. Laboratory studies have primarily addressed embedment kinematics in clay (O'Neill and Randolph, 2001; O'Neill et al., 2003; Chen et al., 2024) and performance in layered clay profiles (Lai et al., 2020) under monotonic loading. The influence of sequential loading on embedment trajectory and pull-out resistance has not been quantified. To address this gap, the study tests how the load order (small–large vs. large–small) and pull-out affect DEA performance. The study also evaluates a practical post-test method for estimating penetration depth by exhumation and three-dimensional (3D) scanning, following the approach demonstrated in sand by Dao et al. (2024, 2025).

2 TEST SETUP

This study comprised four drag embedment anchor (DEA) tests in the Deltares GeoCentrifuge conducted with two clay samples under different loading conditions. Figure 1 shows the experimental setup. A load cell measured the pull force to determine anchor force. After each test, the anchor remained in the container. The sample was dissected to locate void traces left by the fluke tip. The coordinates of the traces were measured from 3D scans of the dissected cross-sections in the point-cloud software CloudCompare to approximate the trajectory of the anchor. Table 1 summarises the conducted tests.

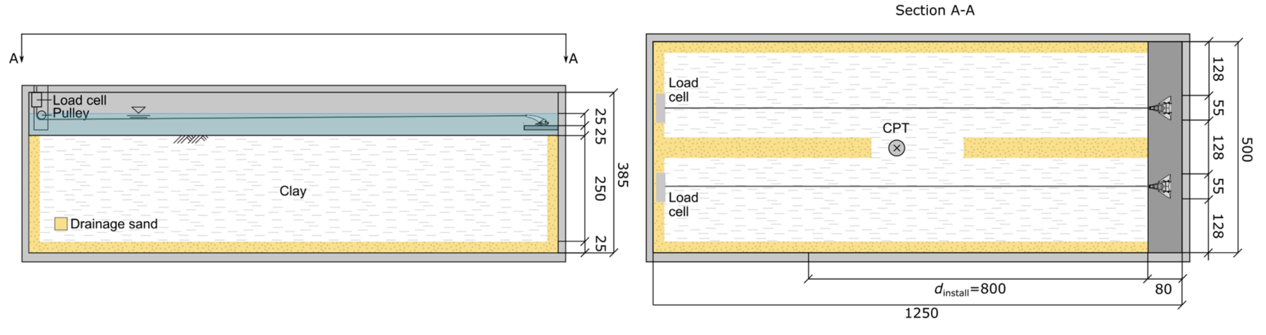

Figure 1: Experimental setup in the test box for clay with measurements in mm

3 ANCHOR MODELS

Figure 2 shows the used DEA model which was roughly based on a Stevshark Rex. The model had a minimum thickness of 0.7 mm, which exceeds the thickness of the reference anchor when scaled to prototype dimensions. Two 3D-printed stainless-steel models were used, each 60 × 55 × 35 mm, with a mass of 20 g and a fluke–shank angle of 45 °. Each soil sample was used for two anchor drag tests. Dyneema ropes with 3 mm diameter served as mooring lines.

4 SOIL SAMPLES

In total, four soil samples were produced. Samples 1 and 2 were sand samples, and tested and described by Dao et al. (2025). The samples used for this study were Samples 3 and 4 which comprised a fine-grained Kaolin clay mixture prepared to achieve a normally consolidated state (overconsolidation ratio, OCR ≈ 1). Table 2 summarises the index properties of the kaolin clay, and Figure 3 shows the grain-size distribution. The Kaolin slurry was prepared at a water content equal to 2.5 times the liquid limit and preconsolidated at 285 kPa. CPTs were performed during the flight, after the tests, to estimate the undrained shear strength profile (Figure 4). The undrained shear strength increased approximately linearly with depth. The shear strength between 0 and 100 mm was classified as medium stiff clay, and strength below 100 mm as stiff clay, following ASTM D2488 and BS CP-2004. The peak values of the undrained shear strength that the anchor models reached in Samples III and IV were 46.8 kPa and 64.3 kPa, respectively.

5 ANCHOR LOADING

During the tests, a hydraulic cylinder applied an unidirectional pulling load on the mooring line. The DEA tests comprised three pulling phases. In Phase I (installation), the DEA was placed on a plate and pulled at 10 mm/s to initiate embedment at 100*g*. Installation continued by dragging the anchor at 10 mm/s to achieve a drag path of 800 mm. In Phase II (sinusoidal loading), Operational and storm conditions were represented by sinusoidal force histories $F(t)$. $F(t)$ was then converted into displacement inputs $x(t)$, using a linear mapping derived from calibration tests in which the actuator force-displacement relationship was measured with a load cell. Load ranges for the scenarios were determined using the panel code panMare by Schulz et al. (2022). Figure 5 shows the resulting displacement time series. In Phase III (pull-out), after the first two phases, the DEA was pulled out continuously at 1 mm/s until the model reached the end of the test box. Figure 6 summarises the complete loading sequence.

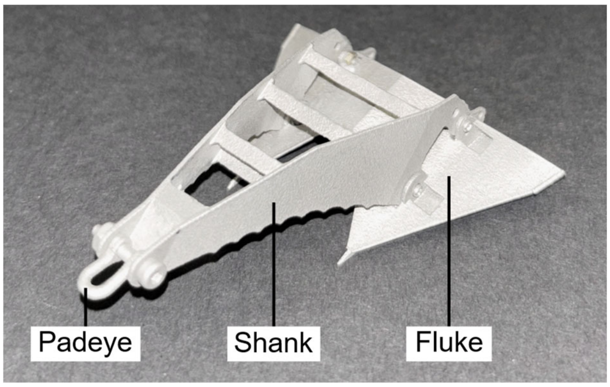

Figure 2: 3D-printed steel anchor model.

Table 1: Test matrix

Test	Sample	Anchor	Phase I	Phase II	Phase III
3a	3	A	Installation	-	Pull-out
3b	3	B	Installation	Storm 1	Pull-out
4a	4	A	Installation	Storm 2	Pull-out
4b	4	B	Installation	Storm 3	Pull-out

Table 2: Kaolin clay properties.

Property	Value
Median particle diameter d_{50} (mm)	0.0076
Liquid limit LL (%)	59.9
Plastic Limit PL (%)	31.2
Specific gravity G_s	2.63
Slope of normal consolidation line λ	0.276
Slope of swelling line κ	0.048
Coefficient of vertical consolidation, c_v (m^2/s) (at OCR = 1 and σ_v' = 30 kPa)	$1.3 \cdot 10^{-7}$

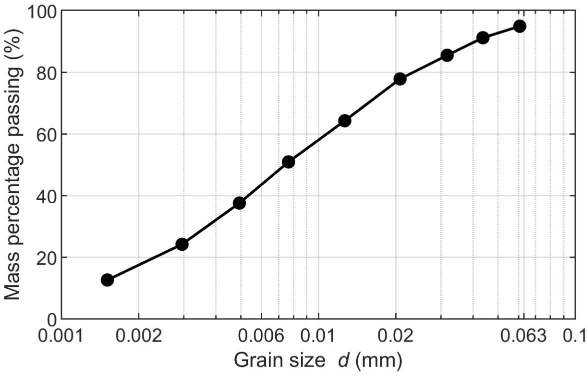

Figure 3: Equivalent grain size distribution of the Kaolin clay.

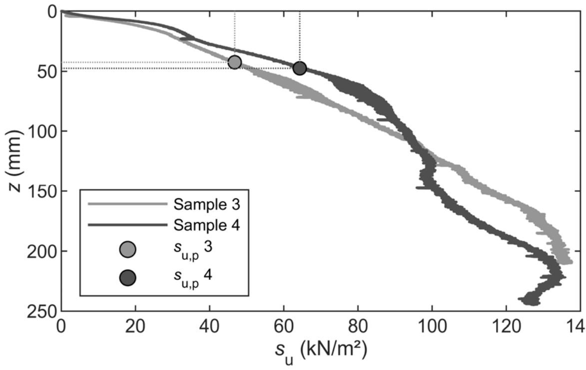

Figure 4: Undrained shear strength profiles of the clay samples.

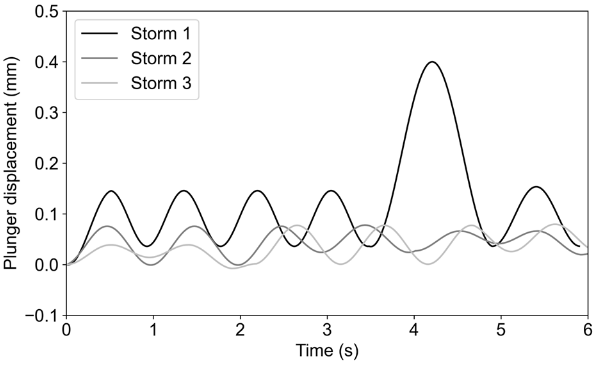

Figure 5: Loading cases for Phase II.

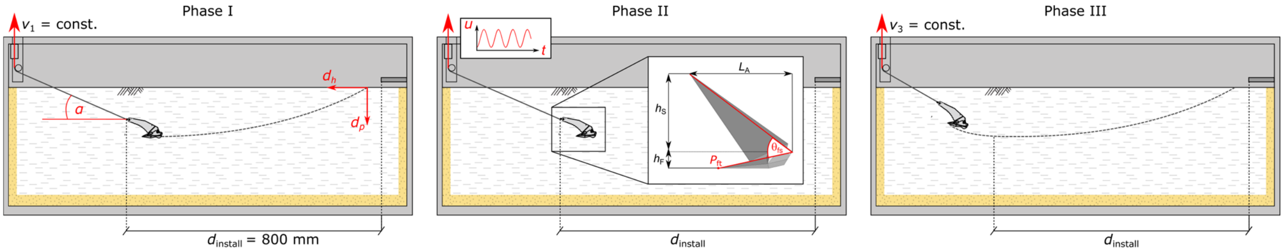

Figure 6: Loading Steps.

6 POST-MEASURING

After each test, the soil sample was drained and sectioned at approximately regular intervals (Figure 7 and Figure 8). 3D surface scans were acquired before and after exhumation using an EinScan HX handheld scanner. Scans were collected in Rapid Scan mode with texture-based alignment and blue light-emitting diode (LED) illumination (Figure 9). The nominal single-scan accuracy was ≤ 0.05 mm with a point spacing of approximately 0.7 mm. Point clouds were registered and converted to a triangular mesh by applying meshing to form connected faces with associated normal vectors and colour. The procedure yielded a coloured 3D mesh aligned with the test axes (Figure 10).

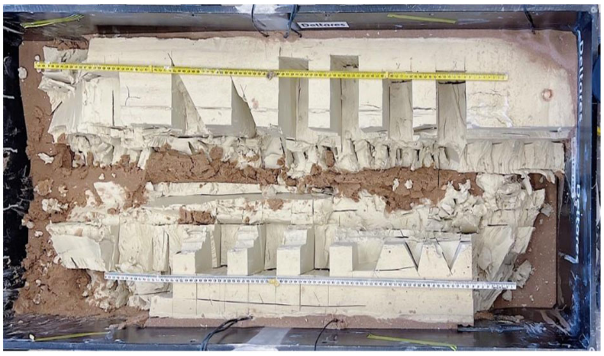

Figure 7: Clay sample after exhumation without anchors.

Figure 8: Clay sample after exhumation without anchors (side view).

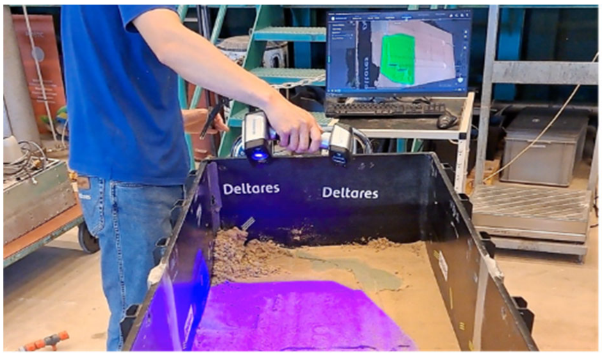

Figure 9: Scanning the soil sample after testing.

7 RESULTS AND ANALYSES

During centrifuge testing, Test 4a recorded a markedly lower anchor force than previous tests. Post-test inspection showed that the anchor rotated onto its back at the mudline instead of remaining embedded (Figure 11). Test 4a was therefore excluded from subsequent analysis. Dropping the anchor from the release platform was required to prevent unwanted and uncontrolled embedment during spin-up and to achieve an initial embedment in the clay, and could therefore not be omitted. The drop height could be reduced by lowering the platform or by preparing a thicker clay layer. Additional control during installation could be achieved by using a stiffer mooring line or by adding lateral guides to the platform to prevent the observed failure.

Figure 12 presents the fluke penetration d_p as a function of the horizontal displacement. Three stages are evident: (1) installation, in which the penetration depth increased up to a horizontal displacement of approximately 13, (2) a quasi-steady stage, in which penetration remained nearly constant up to about 23, and (3) resurfacing, in which the penetration depth decreased. All tests show the same trend during installation. After installation, Test 3a exhibited an earlier and larger loss of penetration depth than the other tests. Tests 3b and 4b behaved similarly during the quasi-steady stage. During resurfacing, the penetration depth responses diverged: Test 3a remained shallowest, followed by Tests 3b and 4b. Despite these differences, all tests converged to similar final penetration depths, indicating a potential stabilisation at high mooring line angles.

The three tests displayed similar patterns of force development, with different peak values as the drag distance increased and the line angle varied. Test 3a (without sinusoidal loading) showed a lower anchor force, even before the Phase II cyclic loading began. The subsequent reduction in force is therefore attributed to limited embedment, rather than to stiffness changes (Figure 13). Application of uniaxial tension in Phase II does not significantly change the force-displacement response.

The anchor-line inclination α increased with towing distance (Figure 13). The angle α was approximated by

$$\alpha \approx \arctan\left(\frac{z_0 + d_\mathrm{p} - h_\mathrm{A}}{x_0 - d_\mathrm{p}}\right) \tag{1}$$

where z_0 denotes the vertical distance between the pulley and the mudline, d_p is the fluke penetration, h_A is anchor height and x_0 is the horizontal distance from the pulley to the initial seabed contact point.

The angle increased approximately linearly up to a horizontal displacement of about 23 and then increased more rapidly. Figure 14 shows the resultant anchor force decomposed into horizontal and vertical components. The horizontal component dominates, but the vertical component remains significant and continues to increase almost linearly. This corresponds to α, even during the stabilisation stage. A 5-minute pause was introduced after the initial pull to allow for set-up effects before Phase II loading. The total and horizontal forces rise steeply to a stable level and then decrease gradually, whereas the vertical force decreases only after reaching its peak.

Figure 15 shows anchor force against penetration depth, with colour intensity indicating horizontal displacement. The anchor force increased with the penetration depth to a maximum and then decreased as resurfacing progresses. This behaviour indicates that the anchor force depends primarily on penetration depth. For the tested model, the force-depth relation is approximated by

$$F/L_\mathrm{f} w_\mathrm{f} s_\mathrm{u,p} = 3.52 \cdot \ln\left(d_\mathrm{p}/L_\mathrm{f} + 1\right). \tag{2}$$

To assess the accuracy of the approximation, the mean absolute percentage error (MAPE) was used. For each observation, the absolute difference between the predicted and measured values was computed as a percentage of the measured value, and the resulting values were averaged across all observations. The result is reported in percent. 0 % denotes a perfect match. The MAPE for Equation 2 is 13.5 %, indicating good agreement with the data.

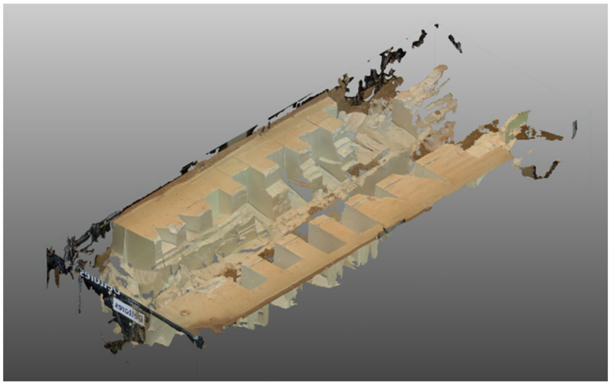

Figure 10: Digitised surface of the dissected soil sample.

Figure 11: Failed Test 4a in which the anchor rotated onto its back.

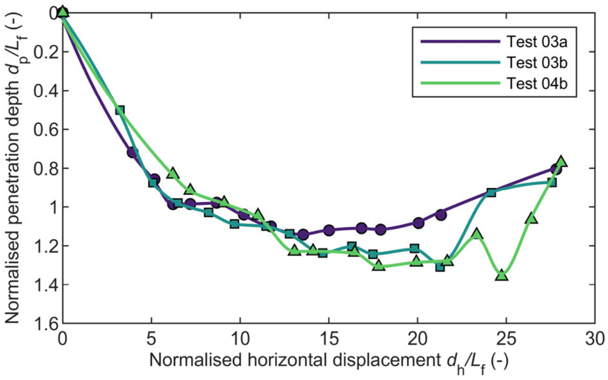

Figure 12: Anchor fluke penetration over horizontal displacement.

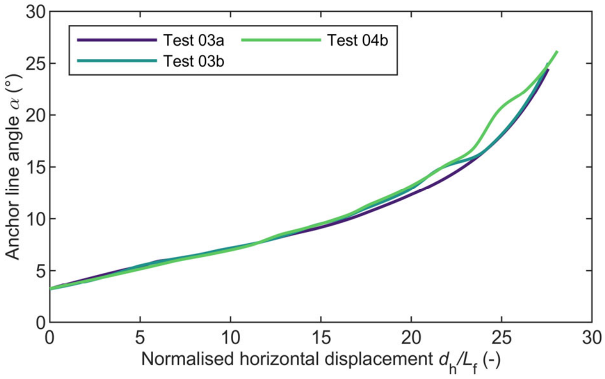

Figure 13: Anchor line angle at padeye over horizontal displacement.

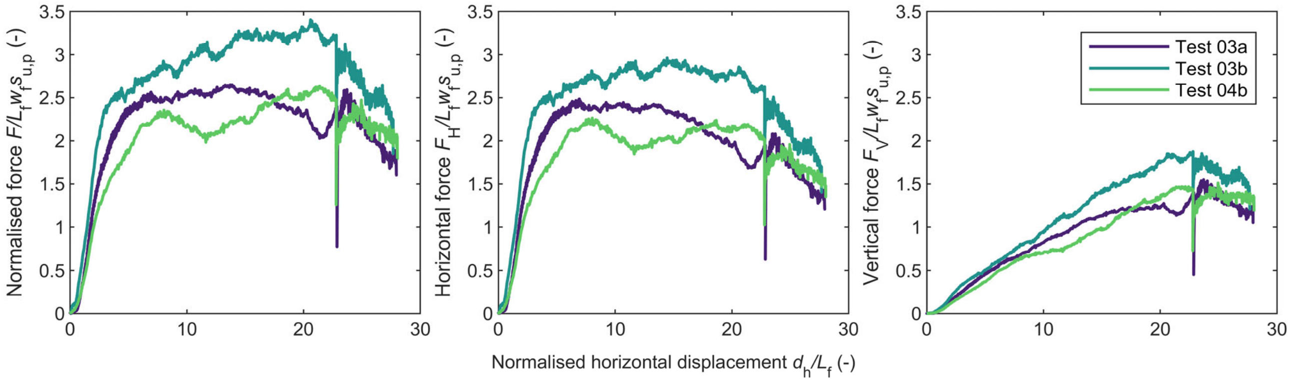

Figure 14: Anchor force as a function of horizontal displacement, showing the total force (left), the horizontal force component (centre), and the vertical force component (right).

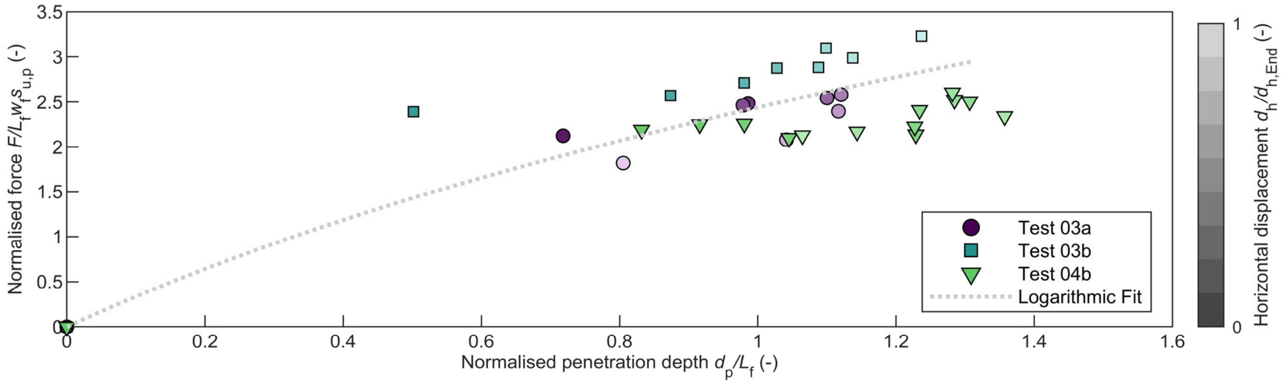

Figure 15: Anchor force vs. penetration depth and quadratic approximation fit.

8 CONCLUSIONS

Four DEA tests were conducted on clay samples in the centrifuge. The tests consisted of three phases – I: installation, II: storm simulation and III: pull-out. The details of Phase II were different for each test. The penetration depth along the drag path was reconstructed by combining exhumation with three-dimensional scanning. Void traces left by the fluke tip were identified in the cross-sections, and the associated *z* coordinate was taken as the maximum depth at each (*x*,*y*) location.

Within these tests, the displacement response was insensitive to the loading sequence of Phase II. Applying a smaller load before a larger one, or the reverse, produced comparable outcomes. This behaviour is consistent with a predominantly elastic load–deformation response. Detecting sequence effects will likely require reversed loading (positive and negative directions) rather than uniaxial tension alone.

The anchor forces throughout the tests correlated primarily with the penetration depth. For the tested model, a logarithmic force-depth relation reproduced the data with a mean absolute percentage error (MAPE) of 0.135.

Overall, the centrifuge results provide a consistent dataset for validation of numerical models.

9 ACKNOWLEDGEMENTS

This project was supported by the Horizon 2020 research program of the European Union within the framework of the GEOLAB project, grant number 101006512, and by the German Research Foundation (DFG) under the funding code GR1024/61-1. We thank John Langstraat, Yao Su, Koen Castelein, Dirk Luger and Rob Zwaan from Deltares for their assistance in planning and carrying out the centrifuge tests. We extend our gratitude to the GEOLAB project partners, Eirini Papapanagiotou from Delmar, and Evelyn Heins from Grundbauingenieure Steinfeld und Partner Beratende Ingenieure mbB, as well as to Victor Remmers from Delmar and Jan Dührkop from Ramboll for their invaluable contributions. We would also like to thank our students, Andrew James Morrison and Katherine Nguyen, for their assistance in conducting and analysing the experiments.

10 REFERENCES

Chen, H., Gao, Y., Shu, S., and Lai, Y. 2023. The six-degree-of-freedom behavior of drag embedment anchor installed in clay. *Ships and Offshore Structures* 19(4), 461-470. doi: 10.1080/17445302.2023.2177029

Cerfontaine, B., White, D., Kwa, K., Gourvenec, S., Knappett, J., and Brown, M. 2023. Anchor geotechnics for floating offshore wind: Current technologies and future innovations. *Ocean Engineering* 279, 114327. doi: 10.1016/j.oceaneng.2023.114327

Dao, D. A., Grabe, J., Peccin da Silva, A., Langstraat, J.H.A., Su, Y. Y., Castelein, K., de Lange, D.A., Luger, D., van Eekelen, S.J.M., and Grabe J. 2024. Dataset: ISEDEA - Influence of Storm Events on Drag Embedment Anchor Behaviour for Floating Offshore Wind Turbines). doi: 10.5281/zenodo.14552391

Dao, D.A., Grabe, J., Peccin da Silva, A., Langstraat, J.H.A., Su, Y.Y., Castelein, K., de Lange, D.A., and van Eekelen, S.J.M. 2025. Centrifuge modelling of anchor performance for floating offshore wind turbines: installation and load behaviour in sand. *Proceedings 5th International Symposium on Frontiers in Offshore Geotechnics (ISFOG)*, Nantes. doi: 10.53243/ISFOG2025-122

Dao, D.A., and Dicke, K. 2024. Numerical investigation of drag embedment anchor model reduction for FOWTs in coarse and fine-grained Baltic Sea soil. *Proceedings 5th International Conference on Geotechnics for Sustainable Infrastructure Development (GEOTEC)*, Hanoi, 2871-2886. doi: 10.1007/978-981-99-9722-0_199

Dao, D.A., Alkateeb, D., and Schröder, M. 2023. Discrepancies between element tests and large-scale LDFE simulations: A case study on anchor kinematics during installation in clay. *Computers and Geotechnics* 163, 105698. doi: 10.1016/j.compgeo.2023.105698

Dao, D.A., and Grabe, J. 2024. Numerical Analysis of Anchor-Chain-Soil Interaction under Operational Loading on Floating Offshore Wind Turbines. *Proceedings 17th Pan-American Conference on Soil Mechanics and Geotechnical Engineering (XVII PCSMGE) and 2nd Latin-American Regional Conference of the International Association for Engineering Geology and the Environment (IAEG)*, La Serena.

Dao, D.A., Struve, A., and Grabe, J. 2022. Numerical Investigation on the Effect of Anchor Modelling on Anchor Chain-Soil Interaction for Floating Offshore Wind Turbines. *Proceedings 15th International Symposium on Practical Design of Ships and other Floating Structures (PRADS)*, Dubrovnik, 1673-1684.

Dao, D.A., Dicke, K., and Grabe, J. 2022. Investigation of anchor installation for floating offshore wind turbines. *Proceedings 10th International Conference on Physical Modelling in Geotechnics*, Daejeon, 482-485).

Gourvenec, S. 2024. Offshore geotechnical challenges of the energy transition. *Geomechanics for Energy and the Environment* 39, 100584. doi: 10.1016/j.gete.2024.100584

Hong, S., McMorland, J., Zhang, H., Collu, M., Halse, K.H. 2024. Floating offshore wind farm installation, challenges and opportunities: A comprehensive survey. *Ocean Engineering* 304. 117793. doi: 10.1016/j.oceaneng.2024.117793

Lai, Y., Zhu, B., Huang, Y., and Chen, C. 2020. Behaviors of drag embedment anchor in layered clay profiles, *Applied Ocean Research* 101, 102287. doi: https://doi.org/10.1016/j.apor.2020.102287

O’Neill, M., and Randolph, M. 2001. Modelling drag anchors in a drum centrifuge. *International Journal of Physical Modelling in Geotechnics* 1(2), 29-41. doi: 10.1680/ijpmg.2001.010203

O'Neill, M.P., Bransby, M.F., and Randolph, M.F. 2003. Drag anchor fluke–soil interaction in clays. *Canadian Geotechnical Journal* 40(1), 78-94. doi: 10.1139/t02-096

Schulz, C.W., Wang, K., Wieczorek, K., Netzband, S., and Abdel-Maksoud, M. 2022. Experimental and numerical investigation of the yaw moment of a downwind coned wind turbine rotor. *Wind Energy* 25(12), 1995-2015. doi: 10.1002/we.2779